Optimization-Based Fundus Image Decomposition for Diagnosis Support of Diabetic Retinopathy

Daichi Kitahara*, Swathi Ananda†, and Akira Hirabayashi*

*College of Information Science and Engineering, Ritsumeikan University, Kusatsu, Shiga, Japan

†Department of Computer Science and Engineering, NMAM Institute of Technology, Nitte, Karkala, Karnataka, India

Abstract—Diabetes mellitus often leads to a serious eye disease called *diabetic retinopathy*, which is one major cause of blindness among adults. Since this blindness can be prevented if the diabetic retinopathy is detected at an early stage and appropriate medical treatment is provided, routine screening tests with fundus images are very important. However, as the number of diabetic patients increases, the routine screening tests are becoming big burdens for ophthalmologists. To reduce these burdens, in this paper, we propose a diagnosis support method by using convex optimization. The proposed method decomposes a green channel fundus image into a basic image composed of non-disease parts, a positive image including exudates, and a negative image including hemorrhages. Numerical experiments show the effectiveness of our method.

I. Introduction

Diabetic retinopathy is a serious eye disease accompanied with diabetes mellitus and a major cause of blindness among working-aged people [1], [2]. Almost all patients with type 1 diabetes and more than 60% of patients with type 2 diabetes get the retinopathy during the first two decades of the disease. On the other hand, it is said that 90% of the blindness caused by the diabetic retinopathy can be prevented if the retinopathy is detected at an early stage and appropriate medical treatment is provided. Therefore, diabetic patients must undergo screening tests regularly to check the onset of the retinopathy.

Fundus photography is the most commonly-used screening for diabetic retinopathy diagnosis. A fundus image of a typical diabetic patient, where the retinopathy has begun to progress, is shown in Fig. 1. In every fundus image, there always exists one optic disc (OD), which is also called the blind spot since there are no photoreceptors in this part. OD represents the beginning of the optic nerve and is shown as a bright circle in the fundus image. Blood vessels (BVs) come into the retina from OD and spread in various directions as capillaries to supply retinal cells with oxygen and nutrition. OD and BVs are non-disease parts included in every fundus image. On the other hand, exudates (EXs) and hemorrhages (HEs) are disease parts included only if the retinopathy develops. Hard EXs are lipid leakages from BV and visible signs of the diabetic retinopathy at an early stage. At the next stage of the retinopathy, soft EXs, which are more blurred compared with hard ones, appear as died and dilated ganglion cell axons. Dot HEs and blot HEs occur from damaged capillaries at an early stage. At the next stage, blood flow is locally stopped, i.e., the ischemia happens, and HEs become larger. When the retinopathy further progresses, abnormal new
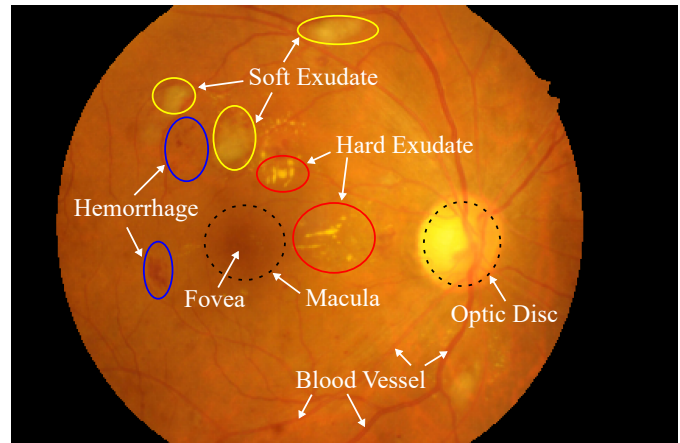
Fig. 1. Typical fundus image. The optic disc, blood vessels, and the macula including the fovea appear in every image as non-disease parts. Hard and soft exudates and hemorrhages appear as disease parts if the retinopathy develops.

BVs are created and then vitreous HEs are caused. Based on the above knowledge, ophthalmologists judge from fundus images whether the diabetic retinopathy develops, progresses, or not.

However, with increasing number of diabetic patients, especially of type 2, the regular screening tests are becoming heavy burdens for the ophthalmologists. To reduce the burdens, many diagnosis support methods have been proposed [3]–[29]. Most of them automatically detect OD, BV, EX, and HE parts from a fundus image through image processing techniques [3]–[13] or machine learning techniques [14]–[27]. These methods return good results for previous datasets, but for a recently released one "Indian diabetic retinopathy image dataset (IDRiD) [30]," their performances seriously degrade. This is because for every fundus image in the previous datasets, the contrast is very high and disease parts are not so large, while in IDRiD, the contrast is low and disease parts of some fundus images are very large.

In this paper, we propose a novel diagnosis support method, which is quite different from all the existing methods [3]–[29]. The propose method decomposes the green channel image of a fundus image into a *basic image* composed of normal areas, a *positive image* including OD & EX, and a *negative image* including BV & HE. The proposed decomposition is expressed as a convex optimization problem, whose constraint is the approximation accuracy for the green channel image, and whose cost function is the sum of convex regularization terms for the basic, positive and negative images. This problem is solved by

(a) Original color image

(b) Red channel image

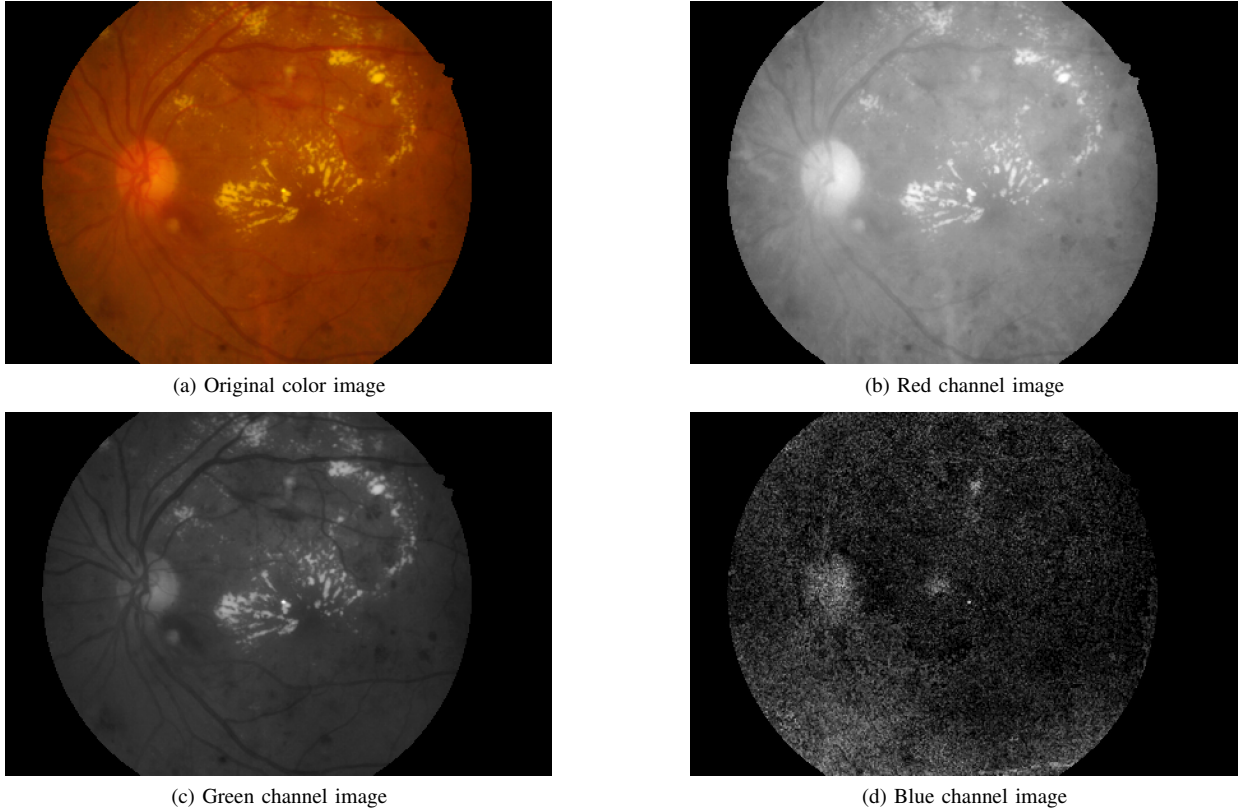

(c) Green channel image

(d) Blue channel image

Fig. 2. Original fundus image and three color channel images. Note that red channel, green channel, and blue channel images are rescaled into $[0, 1]^{I \times J}$.

the primal-dual splitting algorithm [31] introduced in the next section. Experiments using IDRiD demonstrate the effectiveness of the proposed method and its potential for future work.

II. PRIMAL-DUAL SPLITTING ALGORITHM

Let $\mathbb{R}$, $\mathbb{R}_{\geq 0}$, and $\mathbb{R}_{\leq 0}$ be the sets of all real numbers, non-negative real numbers, and non-positive real numbers, respectively. We write a matrix by a capital letter such as $X \in \mathbb{R}^{I \times J}$, and its (i, j)-entry by a small letter with indices i and j such as $x_{i,j} \in \mathbb{R}$. In any finite-dimensional real Hilbert space, $\|\cdot\|_{2,W}$ and $\|\cdot\|_{1,W}$ denote weighted ℓ_2 and ℓ_1 norms, respectively.

Let us consider the following convex optimization problem:

$$\underset{\boldsymbol{x}}{\text{minimize}} \ f(\boldsymbol{x}) + g(\boldsymbol{x}) + h(\mathcal{L}(\boldsymbol{x})), \quad (1)$$

where $\boldsymbol{x} \in \mathcal{X}$ is a vector in a finite-dimensional Hilbert space $\mathcal{X}$, $\mathcal{L} : \mathcal{X} \to \mathcal{Z}$ is a linear mapping to another finite-dimensional Hilbert space $\mathcal{Z}$, $f : \mathcal{X} \to \mathbb{R}$ is a differentiable convex function, and $g : \mathcal{X} \to \mathbb{R} \cup \{\infty\}$ and $h : \mathcal{Z} \to \mathbb{R} \cup \{\infty\}$ are proper lower semicontinuous convex functions.[1] The problem in (1) can be solved by the primal-dual splitting algorithm [31] which iteratively computes, from any initial point $(\boldsymbol{x}^{(0)}, \boldsymbol{\xi}^{(0)}) \in \mathcal{X} \times \mathcal{Z}$,

$$\left\lfloor \begin{array}{l} \boldsymbol{x}^{(t+1)} = \text{prox}_{\gamma_1 g}\big(\boldsymbol{x}^{(t)} - \gamma_1(\nabla f(\boldsymbol{x}^{(t)}) + \mathcal{L}^*(\boldsymbol{\xi}^{(t)}))\big) \\ \boldsymbol{\xi}^{(t+1)} = \text{prox}_{\gamma_2 h^*}\big(\boldsymbol{\xi}^{(t)} + \gamma_2 \mathcal{L}(2\boldsymbol{x}^{(t+1)} - \boldsymbol{x}^{(t)})\big) \end{array} \right. \quad (2)$$

---

[1] A function $f : \mathcal{X} \to \mathbb{R} \cup \{\infty\}$ is called proper, lower semicontinuous, and convex if $\text{dom}(f) := \{\boldsymbol{x} \in \mathcal{X} \mid f(\boldsymbol{x}) < \infty\} \neq \varnothing$, $\text{lev}_{\leq \alpha}(f) := \{\boldsymbol{x} \in \mathcal{X} \mid f(\boldsymbol{x}) \leq \alpha\}$ is closed for all $\alpha \in \mathbb{R}$, and $f(\lambda \boldsymbol{x} + (1 - \lambda)\boldsymbol{y}) \leq \lambda f(\boldsymbol{x}) + (1 - \lambda)f(\boldsymbol{y})$ for all $\boldsymbol{x}, \boldsymbol{y} \in \mathcal{X}$ and all $\lambda \in (0, 1)$, respectively.

for $t \geq 0$, where $\gamma_1 > 0$, $\gamma_2 > 0$, $\mathcal{L}^* : \mathcal{Z} \to \mathcal{X}$ is the adjoint operator of $\mathcal{L}$, and $\text{prox}_{\gamma_1 g} : \mathcal{X} \to \mathcal{X}$ and $\text{prox}_{\gamma_2 h^*} : \mathcal{Z} \to \mathcal{Z}$ are the *proximity operators*[2] of $\gamma_1 g$ and $\gamma_2 h^*$. Note that γ_1 and γ_2 have to satisfy $\frac{1}{\gamma_1} - \gamma_2 \|\mathcal{L}\|_{\text{op}}^2 > \frac{\kappa}{2}$, where $\|\mathcal{L}\|_{\text{op}}$ is the operator norm of $\mathcal{L}$, and $\kappa \geq 0$ is a Lipschitz constant of ∇f.

On the square of a weighted ℓ_2 norm, its proximity operator can be computed for each component by

$$\text{prox}_{\gamma \|\cdot\|_{2,W}^2}(\boldsymbol{y}) = \left(\frac{y_i}{1 + 2\gamma w_i}\right)_i, \quad (3)$$

where w_i is a weight for the ith component y_i. On a weighted ℓ_1 norm, its proximity operator can be computed by

$$\text{prox}_{\gamma \|\cdot\|_{1,W}}(\boldsymbol{y}) = \big(\max(|y_i| - \gamma w_i, 0) \, \text{sgn}(y_i)\big)_i, \quad (4)$$

where $\text{sgn}(y) = 1$ if $y \geq 0$ and $\text{sgn}(y) = -1$ otherwise.

## III. FUNDUS IMAGE DECOMPOSITION VIA OPTIMIZATION

A. Image Decomposition for Diabetic Retinopathy Diagnosis

Original fundus photographs are color images as shown in Fig. 2(a). Figures 2(b), 2(c), and 2(d) show red channel, green channel, and blue channel images of Fig. 2(a), respectively. From Fig. 2(b), we can see that the red channel image is too bright and some components are saturated. From Fig. 2(d), we
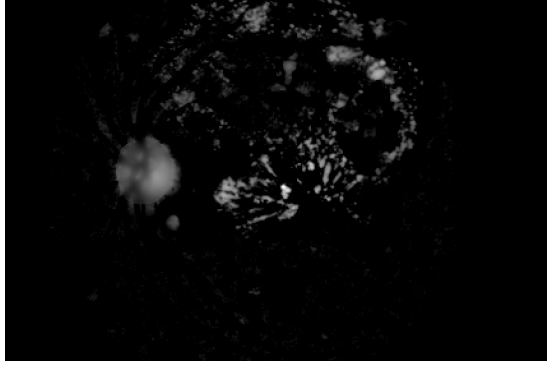
---

[2] For a proper lower semicontinous convex function $f : \mathcal{X} \to \mathbb{R} \cup \{\infty\}$ and any $\gamma > 0$, the proximity operator is defined by $\text{prox}_{\gamma f} : \mathcal{X} \to \mathcal{X} : \boldsymbol{y} \mapsto \text{argmin}_{\boldsymbol{x} \in \mathcal{X}} \gamma f(\boldsymbol{x}) + \frac{1}{2}\|\boldsymbol{x} - \boldsymbol{y}\|_2^2$. In addition, the proximity operator of the conjugate function f^* can be given by $\text{prox}_{\gamma f^*}(\boldsymbol{y}) = \boldsymbol{y} - \gamma \text{prox}_{\frac{1}{\gamma}f}(\frac{1}{\gamma}\boldsymbol{y})$.
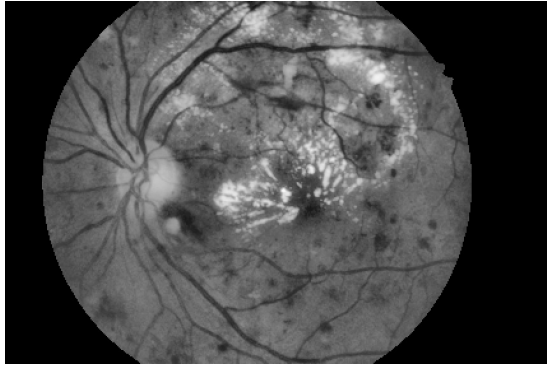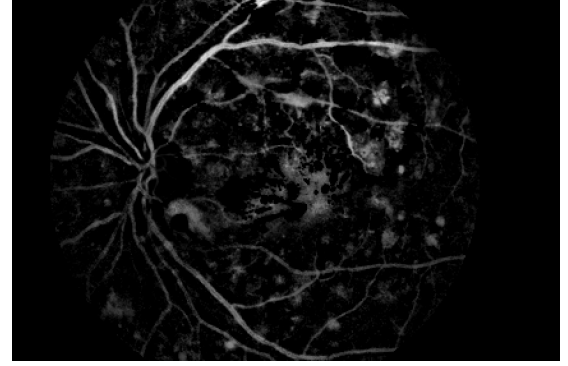
(a) Contrast-enhanced green channel image Y
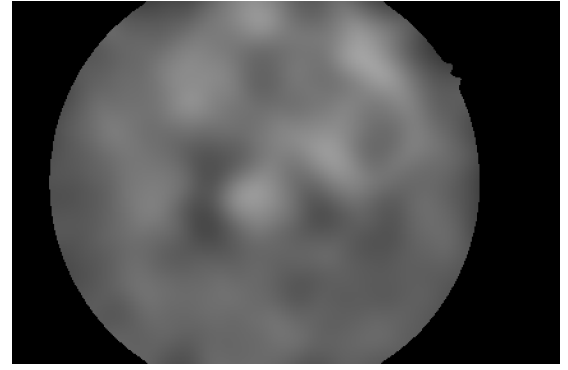
(b) Basic image B composed of only non-disease areas

(c) Positive image P including OD and EX parts

(d) Negative image N including BV and HE parts

Fig. 3. Proposed fundus image decomposition for IDRiD_25. Note that P is rescaled into $[0,1]^{285\times429}$ and N is reversed and rescaled into $[0,1]^{285\times429}$.

can see that the blue channel image is too dark and hence large noise is included. Therefore, as with some methods [4]–[12], we extract the green channel image in Fig. 2(c) from the color image, and use it only for diabetic retinopathy diagnosis.

Although the green channel image appropriately preserves the characteristics of the original color image, its contrast is very different depending on the photographic environment and sometimes not so good as shown in Fig. 2(c). Hence, first, we create a *contrast-enhanced green channel image* $Y \in [0,1]^{I\times J}$ by contrast limited adaptive histogram equalization (CLAHE) [32], and we try to detect OD, BV, EX, and HE parts from Y. By staring at the contrast-enhanced image Y, we can find that OD and EX parts are very bright compared with neighboring pixels. Similarly, BV and HE parts are darker than neighboring pixels. Based on this viewpoint, we propose to decompose Y into a *basic image* $B \in \mathbb{R}^{I\times J}$ as shown in Fig. 3(b), a *positive image* $P \in \mathbb{R}^{I\times J}_{\geq 0}$ in Fig. 3(c), and a *negative image* $N \in \mathbb{R}^{I\times J}_{\leq 0}$ in Fig. 3(d) by solving a convex optimization problem

$$\underset{B,P,N}{\text{minimize}} \ \ \Phi(B) + \Psi(P) + \Omega(N)$$

s.t. $-\epsilon^{\mathrm{n}}_{i,j} \leq b_{i,j} + p_{i,j} + n_{i,j} - y_{i,j} \leq \epsilon^{\mathrm{p}}_{i,j}$, $p_{i,j} \geq 0$ and $n_{i,j} \leq 0$.
(5)

Here $\epsilon^{\mathrm{p}}_{i,j} \geq 0$ and $\epsilon^{\mathrm{n}}_{i,j} \geq 0$ are acceptable errors, of positive and negative directions, from $y_{i,j}$. Three functions Φ, Ψ, and Ω are convex regularization terms for the images B, P, and N.

In this paper, we assume that image and OD masks can be obtained by some preprocessing as shown in Fig. 4. The image mask in Fig. 4(a) can be simply obtained by binarization of the

green channel image in Fig. 2(c) with a fixed threshold. On the other hand, the OD mask in Fig. 4(b) cannot be obtained by simple thresholding, but relatively easily obtained by machine learning methods [14]–[16] since there exists only one OD in every fundus image, and every shape is similar to each other.

By using the above two masks, we define Φ, Ψ, and Ω. The basic image B is smooth, and this property can be evaluated by

$$\Phi(B) := \|\mathcal{D}_2(B)\|^2_{2,W_{\mathrm{b}}} = \sum_{i=1}^{I-2}\sum_{j=1}^{J} w^{\mathrm{b_{vv}}}_{i,j} |b_{i+2,j} - 2b_{i+1,j} + b_{i,j}|^2$$
$$+ \sum_{i=1}^{I-1}\sum_{j=1}^{J-1} w^{\mathrm{b_{vh}}}_{i,j} |b_{i+1,j+1} - b_{i+1,j} - b_{i,j+1} + b_{i,j}|^2$$
$$+ \sum_{i=1}^{I}\sum_{j=1}^{J-2} w^{\mathrm{b_{hh}}}_{i,j} |b_{i,j+2} - 2b_{i,j+1} + b_{i,j}|^2,$$

where $\mathcal{D}_2 : \mathbb{R}^{I\times J} \to \mathbb{R}^{(I-2)\times J} \times \mathbb{R}^{(I-1)\times(J-1)} \times \mathbb{R}^{I\times(J-2)}$ is the twice difference operator, weights $w^{\mathrm{b_{vv}}}_{i,j}$, $w^{\mathrm{b_{vh}}}_{i,j}$ and $w^{\mathrm{b_{hh}}}_{i,j}$ are positive for differences inside the image mask, and are zeros for the other differences. The positive image P is sparse except for OD part that is constant. This property can be evaluated by

$$\Psi(P) := \|P\|_{1,W_{\mathrm{P1}}} + \|\mathcal{D}_1(P)\|^2_{2,W_{\mathrm{P2}}} = \sum_{i=1}^{I}\sum_{j=1}^{J} w^{\mathrm{p}}_{i,j} |p_{i,j}|$$
$$+ \sum_{i=1}^{I-1}\sum_{j=1}^{J} w^{\mathrm{p_v}}_{i,j} |p_{i+1,j} - p_{i,j}|^2 + \sum_{i=1}^{I}\sum_{j=1}^{J-1} w^{\mathrm{p_h}}_{i,j} |p_{i,j+1} - p_{i,j}|^2,$$

where $\mathcal{D}_1 : \mathbb{R}^{I\times J} \to \mathbb{R}^{(I-1)\times J} \times \mathbb{R}^{(I-1)\times J}$ is the first differ-

(a) Image mask

(b) OD mask

Fig. 4. Image mask and OD mask for Y in Fig. 3(a). We assume that these masks are obtained by some preprocessing.

ence operator, a weight $w_{i,j}^{\mathrm{P}}$ is zero in the inside of the OD mask and positive in the other areas, weights $w_{i,j}^{\mathrm{Pv}}$ and $w_{i,j}^{\mathrm{Ph}}$ are positive for differences inside the OD mask, and are zeros for the other differences. The negative image N is also sparse, and this property can be evaluated by

$$\Omega(N) := \|N\|_{1,W_{\mathrm{n}}} = \sum_{i=1}^{I} \sum_{j=1}^{J} w_{i,j}^{\mathrm{n}} |n_{i,j}|,$$

where a weight $w_{i,j}^{\mathrm{n}}$ is always positive and we set the smallest value in the inside of the OD mask because BV is not so dark in this area. Moreover, in the other areas, we recommend to satisfy $w_{i,j}^{\mathrm{n}} \le w_{i,j}^{\mathrm{P}}$. This is because, in the outside of the OD mask, the positive image P is usually more sparse than the negative image N since N always includes BV parts, i.e., non-disease parts, while P only includes EX, i.e., disease parts.

B. Optimization Algorithm

We solve the optimization problem in (5) by the primal-dual splitting algorithm. In (1), by defining $f(B,P,N) := 0$,

$$g(B,P,N) := \begin{cases} 0 & \text{if } (B,P,N) \text{ satisfies all the constraints,} \\ \infty & \text{otherwise,} \end{cases}$$

$$\mathcal{L}(B,P,N) := (\mathcal{D}_2(B), P, \mathcal{D}_1(P), N) =: (Z_1, Z_2, Z_3, Z_4) \text{ and}$$

$$h(\mathcal{L}(B,P,N)) := \|Z_1\|_{2,W_{\mathrm{b}}}^2 + \|Z_2\|_{1,W_{\mathrm{P1}}} + \|Z_3\|_{2,W_{\mathrm{P2}}}^2 + \|Z_4\|_{1,W_{\mathrm{n}}},$$

we construct an optimization problem equivalent to the problem in (5). Then, since $\boldsymbol{x} = (B,P,N)$, $\boldsymbol{\xi} = (Z_1, Z_2, Z_3, Z_4)$, $\mathcal{L}^*(Z_1, Z_2, Z_3, Z_4) = \mathcal{D}_2^*(Z_1) + Z_2 + \mathcal{D}_1^*(Z_3) + Z_4$, and $\mathrm{prox}_{\gamma_2 h^*}$ is computed from (3), (4) and Footnote 2, we can apply the algorithm in (2) if $\mathrm{prox}_{\gamma_1 g}$, i.e., the *projection onto the constraint set*, is computable. We newly elucidated this projection and it can be computed as follows (see Appendix for proof).

For simplicity, define $\widehat{B} := B^{(t)} - \gamma_1 \mathcal{D}_2^*(Z_1^{(t)})$, $\widehat{P} := P^{(t)} - \gamma_1(Z_2^{(t)} + \mathcal{D}_1^*(Z_3^{(t)}))$ and $\widehat{N} := N^{(t)} - \gamma_1 Z_4^{(t)}$. Hence we have $(B^{(t+1)}, P^{(t+1)}, N^{(t+1)}) = \mathrm{prox}_{\gamma_1 g}(\widehat{B}, \widehat{P}, \widehat{N})$, and it is computable for each $(b_{i,j}^{(t+1)}, p_{i,j}^{(t+1)}, n_{i,j}^{(t+1)})$. At first, we compute

$$\widetilde{p}_{i,j} := \begin{cases} \widehat{p}_{i,j} & \text{if } \widehat{p}_{i,j} \ge 0, \\ 0 & \text{otherwise,} \end{cases} \quad \text{and} \quad \widetilde{n}_{i,j} := \begin{cases} \widehat{n}_{i,j} & \text{if } \widehat{n}_{i,j} \le 0, \\ 0 & \text{otherwise.} \end{cases}$$

If $-\epsilon_{i,j}^{\mathrm{n}} \le \widehat{b}_{i,j} + \widetilde{p}_{i,j} + \widetilde{n}_{i,j} - y_{i,j} \le \epsilon_{i,j}^{\mathrm{P}}$, we have $b_{i,j}^{(t+1)} = \widehat{b}_{i,j}$,

$p_{i,j}^{(t+1)} = \widetilde{p}_{i,j}$, and $n_{i,j}^{(t+1)} = \widetilde{n}_{i,j}$. Otherwise, we define $q_{i,j} := y_{i,j} + \epsilon_{i,j}^{\mathrm{P}}$ if $\widehat{b}_{i,j} + \widetilde{p}_{i,j} + \widetilde{n}_{i,j} - y_{i,j} > \epsilon_{i,j}^{\mathrm{P}}$, and $q_{i,j} := y_{i,j} - \epsilon_{i,j}^{\mathrm{n}}$ if $\widehat{b}_{i,j} + \widetilde{p}_{i,j} + \widetilde{n}_{i,j} - y_{i,j} < -\epsilon_{i,j}^{\mathrm{n}}$. Then $(b_{i,j}^{(t+1)}, p_{i,j}^{(t+1)}, n_{i,j}^{(t+1)})$ is given by the following conditional branch:

(i) if $2\widehat{n}_{i,j} - \widehat{p}_{i,j} < \widehat{b}_{i,j} - q_{i,j} < 2\widehat{p}_{i,j} - \widehat{n}_{i,j}$

$$\begin{cases} b_{i,j}^{(t+1)} = \widehat{b}_{i,j} + \frac{q_{i,j} - \widehat{b}_{i,j} - \widehat{p}_{i,j} - \widehat{n}_{i,j}}{3} \\ p_{i,j}^{(t+1)} = \widehat{p}_{i,j} + \frac{q_{i,j} - \widehat{b}_{i,j} - \widehat{p}_{i,j} - \widehat{n}_{i,j}}{3} \\ n_{i,j}^{(t+1)} = \widehat{n}_{i,j} + \frac{q_{i,j} - \widehat{b}_{i,j} - \widehat{p}_{i,j} - \widehat{n}_{i,j}}{3} \end{cases}$$

(ii) if $\widehat{b}_{i,j} - q_{i,j} < \widehat{p}_{i,j} \le 2\widehat{n}_{i,j} - \widehat{b}_{i,j} + q_{i,j}$

$$\begin{cases} b_{i,j}^{(t+1)} = \widehat{b}_{i,j} + \frac{q_{i,j} - \widehat{b}_{i,j} - \widehat{p}_{i,j}}{2} \\ p_{i,j}^{(t+1)} = \widehat{p}_{i,j} + \frac{q_{i,j} - \widehat{b}_{i,j} - \widehat{p}_{i,j}}{2} \\ n_{i,j}^{(t+1)} = 0 \end{cases}$$

(iii) if $2\widehat{p}_{i,j} - \widehat{b}_{i,j} + q_{i,j} \le \widehat{n}_{i,j} < \widehat{b}_{i,j} - q_{i,j}$

$$\begin{cases} b_{i,j}^{(t+1)} = \widehat{b}_{i,j} + \frac{q_{i,j} - \widehat{b}_{i,j} - \widehat{n}_{i,j}}{2} \\ p_{i,j}^{(t+1)} = 0 \\ n_{i,j}^{(t+1)} = \widehat{n}_{i,j} + \frac{q_{i,j} - \widehat{b}_{i,j} - \widehat{n}_{i,j}}{2} \end{cases}$$

(iv) if $\widehat{p}_{i,j} \le \widehat{b}_{i,j} - q_{i,j} \le \widehat{n}_{i,j}$

$$\begin{cases} b_{i,j}^{(t+1)} = q_{i,j} \\ p_{i,j}^{(t+1)} = 0 \\ n_{i,j}^{(t+1)} = 0 \end{cases}$$

where note that we do not use $(\widetilde{p}_{i,j}, \widetilde{n}_{i,j})$ but $(\widehat{p}_{i,j}, \widehat{n}_{i,j})$.

Next, as the second line in (2), we compute

$$\begin{cases} Z_1^{(t+1)} = \mathrm{prox}_{\gamma_2\|\cdot\|_{2,W_{\mathrm{b}}}^2}(Z_1^{(t)} + \gamma_2 \mathcal{D}_2(2B^{(t+1)} - B^{(t)})) \\ Z_2^{(t+1)} = \mathrm{prox}_{\gamma_2\|\cdot\|_{1,W_{\mathrm{P1}}}^*}(Z_2^{(t)} + \gamma_2(2P^{(t+1)} - P^{(t)})) \\ Z_3^{(t+1)} = \mathrm{prox}_{\gamma_2\|\cdot\|_{2,W_{\mathrm{P2}}}^2}(Z_3^{(t)} + \gamma_2 \mathcal{D}_1(2P^{(t+1)} - P^{(t)})) \\ Z_4^{(t+1)} = \mathrm{prox}_{\gamma_2\|\cdot\|_{1,W_{\mathrm{n}}}^*}(Z_4^{(t)} + \gamma_2(2N^{(t+1)} - N^{(t)})) \end{cases}$$

by using (3), (4) and Footnote 2. By repeating the updates of (B,P,N) and (Z_1, Z_2, Z_3, Z_4), we solve the problem in (5).

(a) Contrast-enhanced green channel image Y

(b) Basic image B

(c) Positive image P
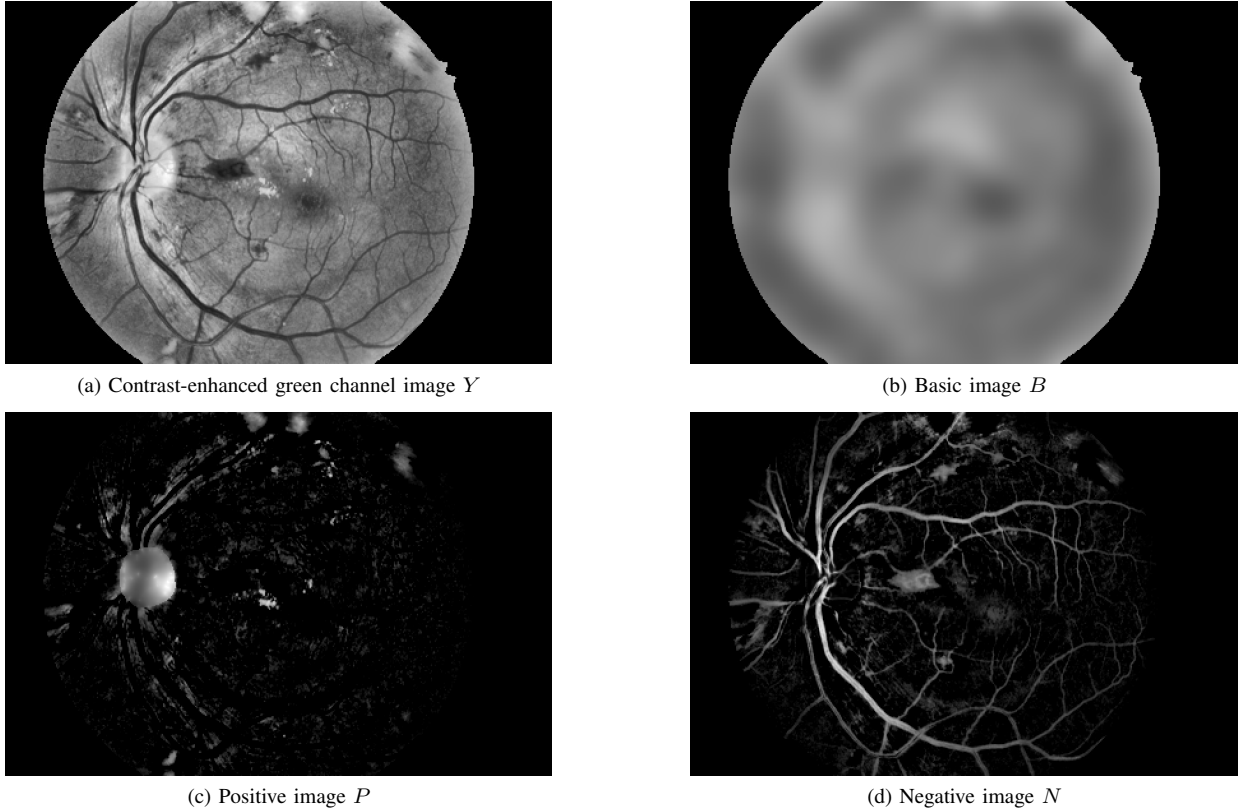

(d) Negative image N

Fig. 5. Proposed fundus image decomposition for IDRiD_31. Note that P is rescaled into $[0, 1]^{285 \times 429}$ and N is reversed and rescaled into $[0, 1]^{285 \times 429}$.

IV. NUMERICAL EXPERIMENTS

A. Experimental Results

We verify the effectiveness of the proposed method by using Indian diabetic retinopathy image dataset[3] [30], which includes fundus images of typical diabetic retinopathy patients. Among all 81 images, we pick up IDRiD_25, IDRiD_31 and IDRiD_66 since the existing strategies do not work well for these images due to low contrast and wide disease areas. As preprocessing, each image mask is created from the normalized green channel image by binarization with a fixed threshold $\frac{20}{255}$, and each OD mask is created by hand. CLAHE is done in MATLAB with ClipLimit $= 0.02$ and Distribution $=$ rayleigh. In the proposed problem in (5), we set $\epsilon_{i,j}^{\mathrm{p}} = 0$ for all (i, j), $\epsilon_{i,j}^{\mathrm{n}} = \frac{5}{255}$ in the inside of the image mask, and $\epsilon_{i,j}^{\mathrm{n}} = 0$ in the outside. Nonzero weights are set to $w_{i,j}^{\mathrm{b_{vv}}} = w_{i,j}^{\mathrm{b_{vh}}} = w_{i,j}^{\mathrm{b_{hh}}} = 25$, $w_{i,j}^{\mathrm{P}} = 0.001$, $w_{i,j}^{\mathrm{P_v}} = w_{i,j}^{\mathrm{P_h}} = 0.025$, $w_{i,j}^{\mathrm{n}} = 0.000125$ in the inside of the OD mask, and $w_{i,j}^{\mathrm{n}} = 0.0005$ in the other areas. The parameter of the primal-dual splitting algorithm is $(\gamma_1, \gamma_2) = (0.15, 0.15)$.

Figures 3, 5, and 6 show the proposed decomposition results for IDRiD_25, IDRiD_31, and IDRiD_66, respectively, where (a) is the contrast-enhanced image Y, (b) is the basic image B, (c) is the positive image P, and (d) is the negative image N. Since the above parameters in (5) are adjusted so that we can obtain good results for IDRiD_25, Figs. 3(c) and 3(d) capture

OD & EX parts and BV & HE parts, respectively. Moreover, from Figs. 5(c), 5(d), 6(c), and 6(d), the proposed method can basically extract OD & EX parts and BV & HE parts as P and N for IDRiD_31 and IDRiD_66. However, in Fig. 5(c), P also captures some non-disease parts, desired to be included in B, especially around BV parts. Similarly, in Fig. 6(d), N captures some non-disease parts especially around EX parts.
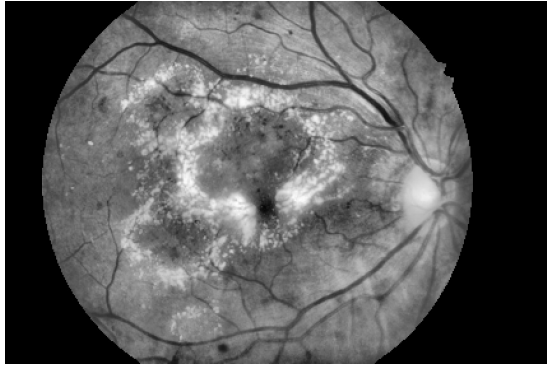
B. Discussion

Through the above experiments, we find that it is dangerous to directly detect EX parts from P and BV & HE parts from N because P and N may include some non-disease parts desired to be in B. Instead of these direct detections, we recommend to use $B + P$ and $B + N$ as shown in Fig. 7(a) and Fig. 7(b), respectively, for each detection. For example, if we would like to extract BV, we should apply some BV extraction method to $B + N$. This is because, even if P and N include some non-disease parts, $B + N$ mainly includes BV, HE and non-disease parts, and hence we can suppers an influence of EX parts.
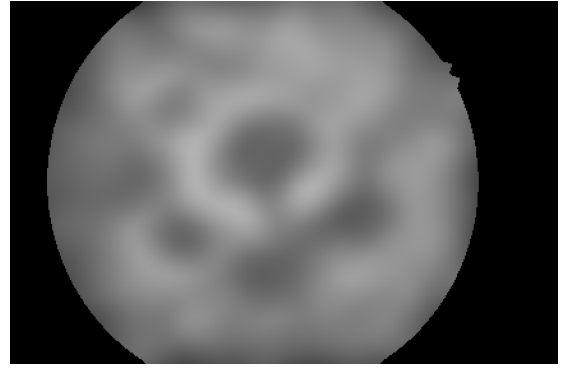
We demonstrate the effectiveness of this strategy by a simple example of BV extraction. We apply the method[4] proposed in [17] to the original image Y in Fig. 3(a) and the recommended one $B+N$ in Fig. 7(b). Figures 8(a) and 8(b) show each results, and from these figures, we can see that the results from $B+N$ is more accurate and the influence of EX parts is suppressed.

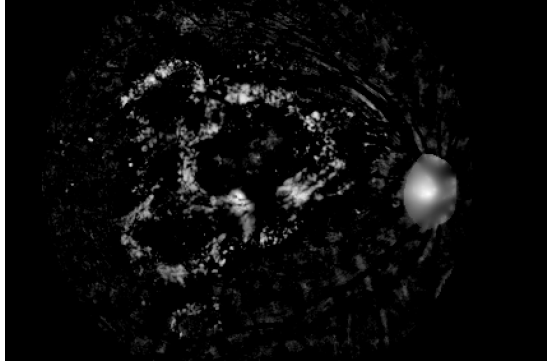[3]URL: https://ieee-dataport.org/open-access/indian-diabetic-retinopathy-image-dataset-idrid

[4]URL: https://www.mathworks.com/matlabcentral/fileexchange/49172-trainable-cosfire-filters-for-curvilinear-structure-delineation-in-images
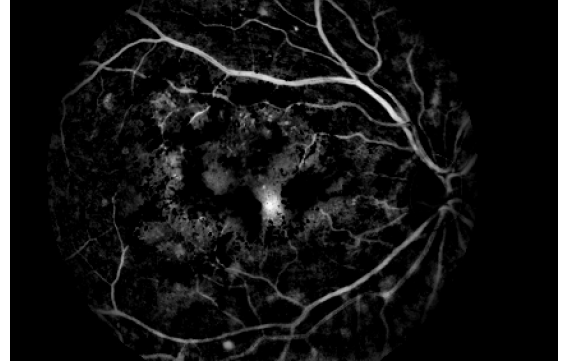
(a) Contrast-enhanced green channel image Y

(b) Basic image B

(c) Positive image P

(d) Negative image N

Fig. 6. Proposed fundus image decomposition for IDRiD_66. Note that P is rescaled into $[0,1]^{285 \times 429}$ and N is reversed and rescaled into $[0,1]^{285 \times 429}$.

V. CONCLUSION

In this paper, we proposed a novel image analysis strategy for fundus photographs of diabetic retinopathy. The proposed method decomposes the contrast-enhanced green channel image into a basic image composed of only non-disease areas, a positive image including OD & EX, and a negative image including BV & HE. The proposed decomposition is formulated as an optimization problem, and it can be solved by the primal-dual splitting algorithm. Experiments using fundus images of typical patients showed the effectivity of the proposed strategy.

APPENDIX
PROJECTION ONTO THE CONSTRAINT SET IN (5)

In Section III-B, the function g is defined by

$$g(B, P, N) := \begin{cases} 0 & \text{if } (B, P, N) \text{ satisfies all the constraints,} \\ \infty & \text{otherwise,} \end{cases}$$

i.e., g is the *indicator function of the constraint set*. For $\widehat{B} \in \mathbb{R}^{I \times J}$, $\widehat{P} \in \mathbb{R}^{I \times J}$, $\widehat{N} \in \mathbb{R}^{I \times J}$ (where $\widehat{P}$ does not need to be positive and $\widehat{N}$ does not need to be negative) and $\gamma > 0$, define

$$(B^*, P^*, N^*) := \text{prox}_{\gamma g}(\widehat{B}, \widehat{P}, \widehat{N}).$$

Then $\text{prox}_{\gamma g}$ is the *projection onto the constraint set* for any γ, and its computation is reduced to the entry-wise problem

$$\underset{b,p,n}{\text{minimize}} \ \frac{1}{2}(b - \widehat{b})^2 + \frac{1}{2}(p - \widehat{p})^2 + \frac{1}{2}(n - \widehat{n})^2 \quad (6)$$
$$\text{s.t. } -\epsilon^{\text{n}} \leq b + p + n - y \leq \epsilon^{\text{p}}, \ p \geq 0 \text{ and } n \leq 0,$$

where the optimal solution (b^*, p^*, n^*) of the problem in (6) corresponds to some entry of (B^*, P^*, N^*).

First of all, from the projection only onto the intersection of the positive and negative constraints, we have

$$\widetilde{p} := \begin{cases} \widehat{p} & \text{if } \widehat{p} \geq 0, \\ 0 & \text{otherwise,} \end{cases} \quad \text{and} \quad \widetilde{n} := \begin{cases} \widehat{n} & \text{if } \widehat{n} \leq 0, \\ 0 & \text{otherwise.} \end{cases}$$

If $-\epsilon^{\text{n}} \leq \widehat{b} + \widetilde{p} + \widetilde{n} - y \leq \epsilon^{\text{p}}$, then $(\widehat{b}, \widetilde{p}, \widetilde{n})$ satisfies all the constrains in (6), and we have $(b^*, p^*, n^*) = (\widehat{b}, \widetilde{p}, \widetilde{n})$ because $(\widetilde{p}, \widetilde{n})$ is given by the projection onto the part of the constraints.

Otherwise, we further modify $(\widehat{b}, \widetilde{p}, \widetilde{n})$ to satisfy the remaining constraint $-\epsilon^{\text{n}} \leq b + p + n - y \leq \epsilon^{\text{p}}$. If $\widehat{b} + \widetilde{p} + \widetilde{n} - y > \epsilon^{\text{p}}$, we only have to decrease the values of $(\widehat{b}, \widetilde{p}, \widetilde{n})$ in order to satisfy $b + p + n - y = \epsilon^{\text{p}}$ because this strategy can minimize the cost function in (6) under all the constraints. Similarly, if $\widehat{b} + \widetilde{p} + \widetilde{n} - y < -\epsilon^{\text{n}}$, we only increase the values of $(\widehat{b}, \widetilde{p}, \widetilde{n})$ to satisfy $b + p + n - y = -\epsilon^{\text{n}}$. Hence, by defining $q := y + \epsilon^{\text{p}}$ if $\widehat{b} + \widetilde{p} + \widetilde{n} - y > \epsilon^{\text{p}}$, and $q := y - \epsilon^{\text{n}}$ if $\widehat{b} + \widetilde{p} + \widetilde{n} - y < -\epsilon^{\text{n}}$, (b^*, p^*, n^*) becomes the solution of the following problem
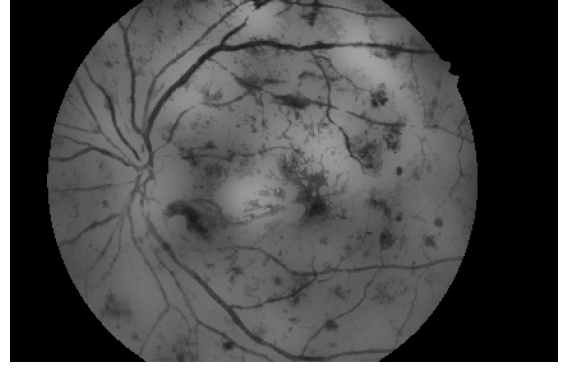
$$\underset{b,p,n}{\text{minimize}} \ \frac{1}{2}(b - \widehat{b})^2 + \frac{1}{2}(p - \widehat{p})^2 + \frac{1}{2}(n - \widehat{n})^2 \quad (7)$$
$$\text{s.t. } p \geq 0, \ n \leq 0 \text{ and } b + p + n = q.$$

To solve the problem in (7), we use the Lagrangian function

$$L(b, p, n, \mu_1, \mu_2, \lambda) := \frac{1}{2}(b - \widehat{b})^2 + \frac{1}{2}(p - \widehat{p})^2 + \frac{1}{2}(n - \widehat{n})^2$$
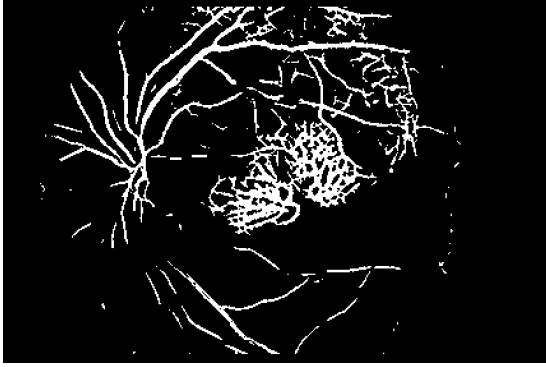$$- \mu_1 p + \mu_2 n + \lambda(q - b - p - n).$$
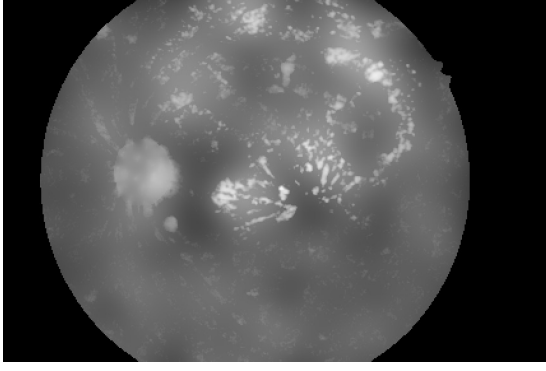
(a) $B + P$ (Fig. 3(b) + Fig. 3(c))

(b) $B + N$ (Fig. 3(b) + Fig. 3(d))

Fig. 7. Recommended images $B + P$ and $B + N$ for detection of EX, BV and HE parts in IDRiD_25. B, P, and N are shown in Figs. 3(b), 3(c), and 3(d).

(a) Results of BV extraction from Y in Fig. 3(a)

(b) Results of BV extraction from $B + N$ in Fig. 7(b)

Fig. 8. Comparison of the BV extraction results by [17] from the contrast-enhanced green channel image Y and the recommend image $B + N$ for IDRiD_25.

Then (b^*, p^*, n^*) satisfies the Karush-Kuhn-Tucker conditions.

- stationarity

$$\begin{pmatrix} b^* - \widehat{b} \\ p^* - \widehat{p} \\ n^* - \widehat{n} \end{pmatrix} = \begin{pmatrix} 0 \\ \mu_1 \\ -\mu_2 \end{pmatrix} + \begin{pmatrix} \lambda \\ \lambda \\ \lambda \end{pmatrix} \quad (8)$$

- primal feasibility

$$\begin{cases} p^* \geq 0 \\ n^* \leq 0 \\ b^* + p^* + n^* = q \end{cases} \quad (9)$$

- dual feasibility

$$\begin{cases} \mu_1 \geq 0 \\ \mu_2 \geq 0 \end{cases} \quad (10)$$

- complementary slackness

$$\begin{cases} \mu_1 p^* = 0 \\ \mu_2 n^* = 0 \end{cases} \quad (11)$$

From (9) and (11), we have

$$p^* > 0 \Rightarrow \mu_1 = 0 \quad \text{and} \quad n^* < 0 \Rightarrow \mu_2 = 0 \quad (12)$$

From (8) and (12), we have $b^* = \widehat{b} + \lambda$,

$$p^* = 0 \text{ or } p^* = \widehat{p} + \lambda > 0 \quad \text{and} \quad n^* = 0 \text{ or } n^* = \widehat{n} + \lambda < 0. \quad (13)$$

From (9) and (13), we have

$$\lambda = \frac{q - \widehat{b} - \widehat{p} - \widehat{n}}{3}, \ \lambda = \frac{q - \widehat{b} - \widehat{p}}{2}, \ \lambda = \frac{q - \widehat{b} - \widehat{n}}{2}, \text{ or } \lambda = q - \widehat{b}.$$

(i) When $\lambda = \frac{q - \widehat{b} - \widehat{p} - \widehat{n}}{3}$, we have

$$\begin{cases} b^* = \widehat{b} + \frac{q - \widehat{b} - \widehat{p} - \widehat{n}}{3} \\ p^* = \widehat{p} + \frac{q - \widehat{b} - \widehat{p} - \widehat{n}}{3} > 0 \\ n^* = \widehat{n} + \frac{q - \widehat{b} - \widehat{p} - \widehat{n}}{3} < 0 \end{cases}$$

and we have $2\widehat{n} - \widehat{p} < \widehat{b} - q < 2\widehat{p} - \widehat{n}$ from the conditions $p^* > 0$ and $n^* < 0$. In this case, the remaining condition in (10) is satisfied because $\mu_1 = \mu_2 = 0$ from (12).

(ii) When $\lambda = \frac{q - \widehat{b} - \widehat{p}}{2}$, we have

$$\begin{cases} b^* = \widehat{b} + \frac{q - \widehat{b} - \widehat{p}}{2} \\ p^* = \widehat{p} + \frac{q - \widehat{b} - \widehat{p}}{2} > 0 \\ n^* = 0 \end{cases}$$

and we have $\widehat{b} - q < \widehat{p} \leq 2\widehat{n} - \widehat{b} + q$ from the condition $p^* > 0$ and the dual feasibility $\mu_2 = \widehat{n} + \lambda \geq 0$ in (10).

(iii) When $\lambda = \frac{q - \widehat{b} - \widehat{n}}{2}$, we have

$$\begin{cases} b^* = \widehat{b} + \frac{q - \widehat{b} - \widehat{n}}{2} \\ p^* = 0 \\ n^* = \widehat{n} + \frac{q - \widehat{b} - \widehat{n}}{2} < 0 \end{cases}$$

and we have $2\widehat{p} - \widehat{b} + q \le \widehat{n} < \widehat{b} - q$ from the condition $n^* < 0$ and the dual feasibility $\mu_1 = -\widehat{p} - \lambda \ge 0$ in (10). (iv) When $\lambda = q - \widehat{b}$, we have

$$\begin{cases} b^* = q \\ p^* = 0 \\ n^* = 0 \end{cases}$$

and we have $\widehat{p} \le \widehat{b} - q \le \widehat{n}$ from the dual feasibility $\mu_1 = -\widehat{p} - \lambda \ge 0$ and $\mu_2 = \widehat{n} + \lambda \ge 0$ in (10).

From the above discussion, we can compute $\text{prox}_{\gamma g}$, i.e., the projection onto the constraint set, as shown in Section III-B.

REFERENCES

[1] D. S. Fong, L. Aiello, T. S. W. Gardner, G. L. King, G. Blankenship, J. D. Cavallerano, F. L. Ferris, and R. Klein, "Retinopathy in diabetes," *Diabetes Care*, vol. 27, no. 1, pp. s84–s87, 2004.

[2] J. W. Y. Yau, S. L. Rogers, R. Kawasaki, E. L. Lamoureux, J. W. Kowalski, T. Bek, S. J. Chen, J. M. Dekker, A. Fletcher, J. Grauslund, S. Haffner, R. F. Hamman, M. K. Ikram, T. Kayama, B. E. K. Klein, R. Klein, S. Krishnaiah, K. Mayurasakorn, J. P. O'hare, T. J. Orchard, M. Porta, M. Rema, M. S. Roy, T. Sharma, J. Shaw, H. Taylor, J. M. Tielsch, R. Varma, J. J. Wang, N. Wang, S. West, L. Xu, M. Yasuda, X. Zhang, P. Mitchell, and T. Y. Wong, "Global prevalence and major risk factors of diabetic retinopathy," *Diabetes Care*, vol. 35, no. 3, pp. 556–564, 2012.

[3] A. M. Mendonça, F. Cardoso, A. V. Sousa, and A. Campilho, "Automatic localization of the optic disc in retinal images based on the entropy of vascular directions," in *Proceedings of the 9th International Conference on Image Analysis and Recognition (ICIAR)*, 2012, pp. 424–431.

[4] B. Gui, R. J. Shuai, and P. Chen, "Optic disc localization algorithm based on improved corner detection," *Procedia Computer Science*, vol. 131, pp. 311–319, 2018.

[5] S. N. Shajahan and R. C. Roy, "An improved retinal blood vessel segmentation algorithm based on multistructure elements morphology," *International Journal of Computer Applications*, vol. 57, no. 16, pp. 31–36, 2012.

[6] S. Shahbeig, "Retinal image analysis using multidirectional functors based on geodesic conversions," *Turkish Journal of Electrical Engineering and Computer Science*, vol. 22, no. 3, pp. 768–779, 2014.

[7] D. O. Dantas, D. de S. Oliveria, and H. D. P. Leal, "Blood vessels extraction using fuzzy mathematical morphology," in *Proceedings of IEEE International Conference on Acoustics, Speech and Signal Processing (ICASSP)*, 2017, pp. 914–918.

[8] P. M. Rokade and R. R. Manza, "Automatic detection of hard exudates in retinal images using Haar wavelet transform," *International Journal of Application or Innovation in Engineering & Management*, vol. 4, no. 5, pp. 402–410, 2015.

[9] M. Zubair, "Automated segmentation of hard exudates using dynamic thresholding to detect diabetic retinopathy in retinal photographs," *Journal of Multimedia Processing and Technologies*, vol. 7, no. 3, pp. 109–116, 2016.

[10] G. B. Kande, T. S. Savithri, and P. V. Subbaiah, "Automatic detection of microaneurysms and hemorrhages in digital fundus images," *Journal of Digital Imaging*, vol. 23, no. 4, pp. 430–437, 2010.

[11] S. B. Júnior and D. Welfer, "Automatic detection of microaneurysms and hemorrhages in color eye fundus images," *International Journal of Computer Science and Information Technology*, vol. 5, no. 5, pp. 21–37, 2013.

[12] P. Bharali, J. P. Medhi, and S. R. Nirmala, "Detection of hemorrhages in diabetic retinopathy analysis using color fundus images," in *Proceedings of IEEE International Conference on Recent Trends in Information Systems (ReTIS)*, 2015, pp. 237–242.

[13] P. J. Navarro, D. Alonso, and K. Stathis, "Automatic detection of microaneurysms in diabetic retinopathy fundus images using the L*a*b color space," *Journal of the Optical Society of America A*, vol. 33, no. 1, pp. 74–83, 2016.

[14] A. Dehghani, H. A. Moghaddam, and M. S. Moin, "Optic disc localization in retinal images using histogram matching," *EURASIP Journal on Image and Video Processing*, vol. 2012, no. 19, 11 pages, 2012.

[15] K. Akyol, B. Şen, and Ş. Bayır, "Automatic detection of optic disc in retinal image by using keypoint detection, texture analysis, and visual dictionary techniques," *Computational and Mathematical Methods in Medicine*, vol. 2016, 10 pages, 2016.

[16] F. Abdali-Mohammadi and A. Poorshamam, "Automatic optic disc center and boundary detection in color fundus images," *Journal of AI and Data Mining*, vol. 6, no. 1, pp. 35–46, 2018.

[17] G. Azzopardi, N. Strisciuglio, M. Vento, and N. Petkov, "Trainable COS-FIRE filters for vessel delineation with application to retinal images," *Medical Image Analysis*, vol. 19, no. 1, pp. 46–57, 2015.

[18] M. Melinščak, P. Prentašić, and S. Lončarić, "Retinal vessel segmentation using deep neural networks," in *Proceedings of the 10th International Conference on Computer Vision Theory and Applications (VISAPP)*, 2015, 6 pages.

[19] M. Ş. Güleryüz and İ. Ulusoy "Retinal vessel segmentation using convolutional neural networks," in *Proceedings of the 26th Signal Processing and Communications Applications Conference (SIU)*, 2018, 4 pages.

[20] P. Prentašić and S. Lončarić, "Detection of exudates in fundus photographs using convolutional neural networks," in *Proceedings of the 9th International Symposium on Image and Signal Processing and Analysis (ISPA)*, 2015, pp. 188–192.

[21] P. Prentašić and S. Lončarić, "Detection of exudates in fundus photographs using deep neural networks and anatomical landmark detection fusion," *Computer Methods and Programs in Biomedicine*, vol. 137, pp. 281–292, 2016.

[22] S. Yu, D. Xiao, and Y. Kanagasingam, "Exudate detection for diabetic retinopathy with convolutional neural networks," in *Proceedings of the 39th Annual International Conference of the IEEE Engineering in Medicine and Biology Society (EMBC)*, 2017, pp. 1744–1747.

[23] R. Zheng, L. Liu, S. Zhang, C. Zheng, F. Bunyak, R. Xu, B. Li, and M. Sun, "Detection of exudates in fundus photographs with imbalanced learning using conditional generative adversarial network," *Biomedical Optics Express*, vol. 9, no. 10, pp. 4863–4878, 2018.

[24] S. Long, X. Huang, Z. Chen, S. Pardhan, and D. Zheng, "Automatic detection of hard exudates in color retinal images using dynamic threshold and SVM classification: Algorithm development and evaluation," *BioMed Research International*, vol. 2019, 13 pages, 2019.

[25] E. Decencière, G. Cazuguel, X. Zhang, G. Thibault, J. C. Klein, F. Meyer, B. Marcotegui, G. Quellec, M. Lamard, R. Danno, D. Elie, P. Massin, Z. Viktor, A. Erginay, B. Laÿ, and A. Chabouis, "TeleOphta: Machine learning and image processing methods for teleophthalmology," *IRBM*, vol. 34, no. 2, pp. 196–203, 2013.

[26] S. S. Rahim, C. Jayne, V. Palade, and J. Shuttleworth, "Automatic detection of microaneurysms in color fundus images for diabetic retinopathy screening," *Neural Computing and Applications*, vol. 27, no. 5, pp. 1149–1164, 2016.

[27] P. Khojasteh, B. Aliahmad, and D. K. Kumar, "Fundus images analysis using deep features for detection of exudates, hemorrhages and microaneurysms," *BMC Ophthalmology* vol. 18, no. 288, 13 pages, 2018.

[28] P. Prasanna, S. Jain, N. Bhagat, and A. Madabhushi, "Decision support system for detection of diabetic retinopathy using smartphones," in *Proceedings of the 7th International Conference on Pervasive Computing Technologies for Healthcare and Workshops*, 2013, pp. 176–179.

[29] A. M. R. R. Bandara and P. W. G. R. M. P. B. Giragama, "A retinal image enhancement technique for blood vessel segmentation algorithm," in *Proceedings of IEEE International Conference on Industrial and Information Systems (ICIIS)*, 2017, 5 pages.

[30] P. Porwal, S. Pachade, R. Kamble, M. Kokare, G. Deshmukh, V. Sahasrabuddhe, and F. Meriaudeau, "Indian diabetic retinopathy image dataset (IDRiD): A database for diabetic retinopathy screening research," *Data*, vol. 3, no. 3, 8 pages, 2018.

[31] L. Condat, "A primal-dual splitting method for convex optimization involving Lipschitzian, proximable and linear composite terms," *Journal of Optimization Theory and Applications*, vol. 158, no. 2, pp. 460–479, 2013.

[32] K. Zuiderveld, "Contrast limited adaptive histogram equalization," in *Graphic Gems IV*, P. S. Heckbert Ed. San Diego, CA: Academic Press, 1994, pp. 474–485.